(This is a sample cover image for this issue. The actual cover is not yet available at this time.)

Earth and Planetary Science Letters 355–356 (2012) 109–118

Contents lists available at SciVerse ScienceDirect

Earth and Planetary Science Letters

journal homepage: www.elsevier.com/locate/epsl

Stratigraphic changes of Ge/Si, REE+Y and silicon isotopes as insights into the deposition of a Mesoarchaean banded iron formation

C. Delvigne [a,b,*], D. Cardinal [b,1], A. Hofmann [c], L. André [a,b]

[a] Department of Earth Sciences and Environment, Université Libre de Bruxelles, Avenue Franklin Roosevelt 50, 1050 Brussels, Belgium
[b] Department of Geology and Mineralogy, Royal Museum of Central Africa, Leuvensesteenweg 13, 3080 Tervuren, Belgium
[c] Department of Geology, University of Johannesburg, PO Box 524, Auckland Park 2006, Johannesburg, South Africa

ARTICLE INFO

Article history:
Received 30 January 2012
Received in revised form
8 July 2012
Accepted 23 July 2012
Editor: T.M. Harrison

Keywords:
silicon isotopes
Ge/Si ratios
banded iron formation
Archaean
Pongola Supergroup

ABSTRACT

In order to determine the origin of silicon (Si) in banded iron formation (BIF), we have undertaken a multi-tracer study combining REE+Y data, Ge/Si ratios and Si isotopes (δ^{30}Si) on stratigraphically resolved layers from a ~2.95 Ga BIF from the Pongola Supergroup, South Africa. Si in both Si-rich and Fe-rich layers has a common origin, represented by a seawater reservoir strongly influenced by continent-derived freshwaters (~10%) and very limited (<0.1%) high-T hydrothermal fluids as indicated by Eu anomalies and Y/Ho ratios. The coevolution of δ^{30}Si signatures of Si- and Fe-rich layers of the BIF coupled with similar Eu and Y anomalies in both types of layers is in accordance with a common silica precipitation promoted by Si adsorption onto Fe-oxyhydroxides from Archaean seawater. An increase in δ^{30}Si values from −2.27‰ to −0.53‰ stratigraphically upwards in the BIF is inferred to be the result of two successive isotopic fractionation processes during (1) silicon adsorption onto the Fe-oxyhydroxide precursor and (2) silica precipitation at the sediment–water interface from pore fluid triggered by the local silica saturation consecutive to an early diagenetic Si desorption from the precursor Fe-oxyhydroxide. The first fractionation process depleted the parental water in ^{28}Si while the second released ^{30}Si back into the parental water, resulting in an increase of the δ^{30}Si value of the parental water reservoir over time.

1. Introduction

The mechanism that gave rise to the precipitation of alternating iron- and silica-rich layers of banded iron formations (BIFs) in the Precambrian is still unresolved despite extensive investigations. Most studies on BIFs have focused on the origin of Fe-rich bands. It is generally accepted that Fe^{2+} was sourced from hydrothermal alteration of oceanic crust (e.g., Jacobsen and Pimentel-Klose, 1988; Derry and Jacobsen, 1990; Bau and Möller, 1993). Proposed mechanisms of oxidation of Fe^{2+} and subsequent precipitation of ferric iron are still debated (Bekker et al., 2010). They include abiotic photo-oxidation (Cairns-Smith, 1978; Braterman et al., 1983), direct oxidation by Fe(II)-oxidizing anoxygenic photoautotrophic bacteria (Konhauser et al., 2002; Kappler et al., 2005; Posth et al., 2008) and abiotic oxidation with cyanobacterially-generated O_2 (Cloud, 1965, 1973).

Silica is regarded to have been derived either from continental sources (Hamade et al., 2003; Frei and Polat, 2007) or seafloor hydrothermal fluids (André et al., 2006; Lascelles, 2007; Steinhoefel et al., 2009; Wang et al., 2009). In the absence of silica-secreting organisms, our current understanding of Precambrian oceans is limited to the assumption that silicon (Si) concentrations were close to saturation of amorphous silica (Siever, 1992). Banding in iron formation has been argued to reflect alternating chemical precipitation of colloidal iron oxyhydroxides and silica (Garrels, 1987) or continuous evaporative silica precipitation with episodic deposition of iron (Morris, 1993). Alternatively to such direct Si precipitation from seawater, Fischer and Knoll (2009) proposed a model where silicic acid adsorbed onto Fe-hydroxide precipitates to form a siliceous ferric oxyhydroxide precursor that sank to the sea floor along with organic matter. In sediments, bacterial oxidation of organic matter and Fe reduction liberated silica that concentrated into pore fluids and ultimately precipitated and transformed into early diagenetic chert. Evaluating the different models requires a better understanding of the source of silicon in BIF.

Ge/Si ratios are useful in this regard, as they may highlight mixing processes between hydrothermally and continentally

* Corresponding author at: Department of Geology and Mineralogy, Royal Museum of Central Africa, Leuvensesteenweg 13, 3080 Tervuren, Belgium. Tel.: +32 2 769 54 60; fax: +32 2 769 54 32.
E-mail address: cdelvign@ulb.ac.be (C. Delvigne).
[1] Now at: Laboratoire d'Océanographie et du Climat, Expérimentations et Approches Numériques, Université Pierre et Marie Curie, Institut Pierre Simon Laplace, Place Jussieu Boîte 100-4, 75252 Paris, France.

0012-821X/$ - see front matter © 2012 Elsevier B.V. All rights reserved.
http://dx.doi.org/10.1016/j.epsl.2012.07.035

derived fluids, both of which display very different Ge/Si ratios (8–14 μmol/mol and 0.54 μmol/mol, respectively; Mortlock et al., 1993; Froelich et al., 1992). Based on the covariation of Ge/Si ratios and silica content of iron formation mesobands, Hamade et al. (2003) and Frei and Polat (2007) argued for mixing scenarios involving two water masses with different geochemical composition that interacted with each other: high Ge/Si bottom seawater strongly impacted by hydrothermal fluids and low Ge/Si surface waters strongly influenced by continental inputs. These authors further considered that silica was predominantly derived from weathering of a continental landmass, whereas iron was sourced from oceanic hydrothermal systems. Their proposal relies on the assumption that Si and Ge do not fractionate during silica precipitation and instead maintain their ratio representative of their source. However, this can be biased by the potential preferential adsorption of Ge onto Fe-oxyhydroxides (Pokrovsky et al., 2006). Moreover, significant fractionation of Ge may take place during inorganic quartz precipitation from hydrothermal fluids (Evans and Derry, 2002).

The fractionation of the stable isotopes of silicon has recently been explored as a tool to study silica sources in Archaean BIFs (André et al., 2006; Steinhoefel et al., 2009, 2010). These studies concluded that negative δ^{30}Si signatures converge with Fe isotopic data in support of a common hydrothermal origin for both elements. Steinhoefel et al. (2009) further suggested that the variability of the Si isotope composition might reflect modifications of hydrothermal fluids with distance to the venting site caused by Rayleigh distillation and/or mixing with ambient seawater.

In an attempt to decipher amongst different processes that may have controlled Si precipitation of Archaean BIFs, we have undertaken a multi-tracer study combining REE+Y data, Ge/Si ratios and Si isotopes (δ^{30}Si) on stratigraphically resolved layers sampled in a 2.95 Ga BIF from the Pongola Supergroup, South Africa. The very good stratigraphic control is used here to investigate time-related controls of silica precipitation within both Si- and Fe-rich layers and deduce a coherent scenario for Archaean BIF deposition.

2. Geological setting and sample locations

The Mesoarchaean Pongola Supergroup is a volcano-sedimentary sequence that was deposited ca. 3.0–2.85 Ga ago on the southeastern margin of the Kaapvaal Craton. It is exposed in the Mpumalanga and KwaZulu-Natal provinces of South Africa and Swaziland, and can be partly correlated with the Witwatersrand Supergroup of South Africa (Beukes and Cairncross, 1991). The Pongola Supergroup comprises two stratigraphic units: a lower volcano-sedimentary Nsuze Group and an upper, largely sedimentary Mozaan Group. The base of the Mozaan Group is represented by the Sinqeni Formation that was studied in the White Mfolozi Inlier (coordinates S28°13.881; E031°11.813). The Sinqeni Formation consists of two major sandstone units separated by a ca. 12 m thick succession of mudrock and BIF referred to as the Vlakhoek Member. A lower silt-rich mudrock unit grades upwards into clay-rich mudrock (Dix, 1984) and displays ripple marks at the sampled outcroup. Overlying the mudrock is a 3 m thick unit of jaspilitic BIF from which the samples originate. The BIF consists of jasper pods and bands alternating with magnetite-haematite mesobands (Beukes and Cairncross, 1991). This iron formation is, in turn, overlain by green mudrocks (Dix, 1984). BIFs of the Pongola Supergroup have been deposited in an epicontinental sea, on a shallow, sediment-starved outer continental shelf during peaks in marine transgressions (Matthews, 1967; von Brunn and Mason, 1977; Tankard et al., 1982; Beukes and Cairncross, 1991). The metamorphic grade of the Pongola Supergroup is lower greenschist facies (Hammerbeck, 1977; Linström, 1987). Deposition of the Mozaan Group is constrained by the age of Nsuze Group lavas at 2985 ± 1 Ma (U–Pb single zircon; Hegner et al., 1994) and the age of intrusion of "post-Pongola granites" the oldest of which, the Godlwayo Granite, has been dated at 2863 ± 8 Ma (Pb–Pb zircon evaporation; Reimold et al., 1993).

3. Analytical techniques

Rocks were collected from surface exposure without obvious weathering, i.e. major changes in colour or texture. Exposed surfaces were cut to avoid contributions of any weathering rinds and Si-rich and Fe-rich mesobands were separated by sawing before grinding. Samples were then reduced into small chips (2–5 mm) with a rock hammer. To avoid any contamination in Ge, REE+Y and Si isotopic signature, between 10 and 40 g of samples were powdered using a tungsten carbide grinding bowl. Powders were dried in an oven overnight at 100 °C.

For major and trace element contents, about 50 mg of powdered rock samples were dissolved by lithium metaborate fusion with 99.999% purity (American Element) at 1000 °C for 1 h in platinum crucibles. The 1:3 flux to sample ratio for Si-rich samples was increased to 1:8 to achieve complete dissolution of Fe-rich samples. The fusion beads were dissolved in 5% HNO_3 and the solutions were analysed for major elements, Ge and REE+Y contents.

Major elements compositions were measured by ICP-AES (Iris Advantage) with gold (Au) and yttrium (Y) as internal standards. All calibration standards and samples were matrix matched using the appropriate flux to sample ratio to avoid any matrix effect. Typical accuracy of ICP-AES analysis was ± 2% for major elements and ± 5% for elements below 2 wt% (Al, Ca, K, Mg, Mn, Na, P and Ti) as checked using geostandards SGR-1 (shale) and a 5 ppm artificial multi-element solution standard. Using geostandards IF-G (BIF), accuracy of ICP-AES analysis was ± 5% for major elements and ± 10% for elements below 2 wt% (Al, Ca, K, Mg, Mn, Na, P and Ti).

Ge and REE+Y concentrations were analysed by HR-ICP-MS (Element 2) in low-resolution mode with indium (In) as internal standard (Robinson et al., 1999). Detection limits are given in Table 1. Typical accuracy for Ge is ± 1–2% (checked with geostandard IF-G). Specific BaO interference on Eu and PrO and CeOH interferences on Gd were corrected following Aries et al. (2000) calculations with Th (a 0.5 ppb Th spike was added to all samples) as the normalizing element. Typical accuracy is better than 5% for Y, Ba, La, Ce, Pr, Gd, Tb, Dy, Ho, Er, Yb and Lu and below 10% for Nd, Eu and Sm (checked with geostandard IF-G and a 0.1 ppb artificial multi-element solution).

For Si isotopes a NaOH alkaline attack and chromatographic purification was carried out following the procedure of Georg et al. (2006). To achieve complete dissolution (particularly for Fe-rich samples), only 1–5 mg of powdered rock was used (Fitoussi et al., 2009). Since a shift of up to 0.4‰ in measured δ^{30}Si can occur due to a slight decrease in pH of the solution loaded on the cationic exchange resin (Fitoussi et al., 2009), we adjusted all solution to a pH 2 before the cationic purification step.

Si isotopic ratios were then measured in at least duplicate using a Nu Plasma multicollector plasma source mass spectrometer (MC-ICP-MS) operating in dry plasma mode, with an external Mg doping to correct mass bias (Cardinal et al., 2003; Abraham et al., 2008). Data were obtained by the sample-standard bracketing technique relative to the NBS-28 silica sand standard for silicon isotopes. Since Van den Boorn et al. (2009) reported significant offsets in MC-ICP-MS silicon-isotope measurements induced by the presence of sulphur, a SO_4^{2-} spike

Table 1
Major element (wt%) and selected trace elements (ppb, unless other specified) concentrations, Ge/Si ratios and silicon isotopic compositions for individual mesobands of BIFs from the Mozaan Group. The term 'bulk' states for a whole Si-rich mesoband (e.g., PG-1 bulk) that was subdivided in subsamples (e.g., PG-1A, 1B, 1C, 1D) without any Fe-rich mesoband intercalated between them. ADL is the analytical detection limit in rock calculated as 10sd on 10 procedural blanks with a sample flux ratio of 1:3 for Si-rich mesobands and 1:8 for Fe-rich mesobands. Sd is one standard deviation of δ^{30}Si replicates.

Sample	**LDA**	**LDA**	**PG-1A**	**PG-1B**	**PG-1C**	**PG-1D**	**PG-1bulk**	**PG-2A**	**PG-2C**	**PG-2D**	**PG-3**	**PG-4A**	**PG-4B**	**PG-5A**	**PG-5B**	**PG-5C**	**PG-6B**	**PG-6C**	**PG-7A**	**PG-7B**	**PG-7C**	**PG-7D**	**PG-7E**	**PG-7bulk**	**PG-8**	**PG-9**
	Si-rich	Fe-rich	Si-rich	Si-rich	Si-rich	Si-rich	Si-rich	Si-rich	Si-rich	Si-rich	Fe-rich	Fe-rich	Fe-rich	Si and Fe-rich	Si-rich	Fe-rich	Si-rich	Fe-rich	Si-rich	Si-rich	Si-rich	Si-rich	Si and Fe-rich	Si-rich	Fe-rich	Si-rich
Metres below top of sequence			0.025	0.055	0.08	0.1	0.05	0.15	0.23	0.3	0.4	0.85	0.9	1	1.05	1.15	1.2	1.3	1.41	1.445	1.48	1.52	1.55	1.48	1.9	2.05
SiO_2			81.1	85.7	80.8	76.3	83.7	88.4	86.1	87.2	27.8	33.5	37.0	49.6	88.6	29.3	87.2	32.6	98.1	97.6	84.3	84.4	48.4	91.1	19.5	73.4
Al_2O_3			< ADL	< ADL	0.00	< ADL	< ADL	< ADL	< ADL	0.06	0.55	0.69	1.24	0.60	0.31	0.04	0.28	0.05	0.13	0.06	< ADL	0.24	0.45	0.18	0.42	< ADL
$Fe_2O_{3\ TOT}$			16.2	6.4	13.3	19.2	14.4	8.1	7.4	6.5	70.2	64.2	58.1	42.4	9.7	66.8	12.8	67.6	5.3	2.4	6.2	9.1	44.0	5.9	73.4	25.2
MnO			1.16	0.33	1.07	2.33	1.45	0.39	0.88	0.75	0.66	0.54	1.16	0.26	0.16	0.12	0.14	0.08	0.32	0.04	0.07	0.41	1.28	0.25	1.25	1.35
MgO			0.02	0.01	0.02	0.03	0.03	0.03	0.03	0.02	0.09	0.05	0.10	0.03	0.10	< ADL	0.03	< ADL	0.02	0.02	0.01	0.04	0.05	0.02	0.12	0.08
CaO			0.04	0.03	0.06	0.04	0.03	0.04	0.02	0.03	0.03	0.05	0.05	0.04	0.10	0.03	0.03	0.04	0.02	0.01	0.05	0.03	0.05	0.03	0.12	0.04
Na_2O			0.02	0.09	0.03	0.05	0.12	0.08	0.12	0.10	0.09	0.03	0.01	0.02	0.04	0.02	< ADL	0.05	0.02	0.06	0.09	0.10	0.00	0.02	0.09	0.01
TiO_2			0.22	< ADL	< ADL	< ADL	0.11	0.14	< ADL	0.01	0.22	0.71	1.14	< ADL	0.02	0.26	< ADL	< ADL	0.15	0.11	< ADL	0.14	0.07	< ADL	0.20	< ADL
P_2O_5			0.15	0.20	0.14	0.13	0.11	0.08	0.06	0.11	0.28	0.20	0.27	0.12	< ADL	0.14	0.14	0.06	0.07	0.15	0.11	0.20	0.19	0.15	0.15	0.12
Total			98.9	92.8	95.5	98.1	99.9	97.3	94.6	94.8	99.9	100.0	99.1	93.1	99.0	96.8	100.6	100.5	104.1	100.4	90.8	94.6	94.6	97.6	95.3	100.2
Ba	1823	2577	1915	< ADL	< ADL	< ADL	7764	2119	12974	< ADL	3392	2630	< ADL	< ADL	< ADL	4075	< ADL	< ADL	2010	< ADL	< ADL	< ADL	3373	< ADL	66834	121911
La	33	2016	359	154	268	839	341	153	275	250	5518	3081	3151	1572	1017	2407	430	2359	2751	580	360	851	1784	1265	2053	834
Ce	43	30	588	195	382	1044	511	199	294	364	10049	4898	5538	2671	1641	3690	709	3322	4609	957	606	1346	3031	1659	3224	938
Pr	1	2	73	21	43	112	63	23	48	43	1165	538	640	320	182	403	84	363	501	105	68	148	352	181	371	172
Nd	4	9	287	83	172	426	251	86	177	166	4498	2041	2642	1267	662	1484	326	1275	1665	363	266	536	1373	641	1423	673
Sm	1	2	68	23	43	88	60	27	37	40	1003	434	698	301	116	267	75	208	213	52	50	93	317	99	289	152
Eu	1	34	33	13	22	48	30	13	19	23	371	198	329	167	54	132	39	106	83	22	23	41	174	44	124	79
Gd	5	130	68	35	59	118	59	27	41	44	1046	491	771	272	83	241	60	162	116	32	43	78	301	70	325	145
Tb	0	5	13	5	9	14	11	6	8	9	152	65	109	53	15	34	12	31	23	7	9	15	59	14	48	28
Dy	1	5	80	33	61	88	71	36	55	59	900	374	647	302	79	182	70	155	92	31	45	79	338	70	301	171
Y	5	107	922	436	794	1147	817	468	582	561	6033	2780	4162	1830	514	977	480	996	769	258	390	638	2533	522	2562	1550
Ho	0	1	19	8	15	24	17	9	13	14	208	95	153	64	16	37	15	33	20	7	10	17	75	14	76	38
Er	1	3	47	21	38	69	44	24	32	36	504	240	386	166	41	102	36	84	56	16	23	45	190	36	194	94
Yb	18	394	42	< ADL	33	36	25	< ADL	27	36	< ADL	< ADL	< ADL	133	28	< ADL	33	< ADL	28	< ADL	23	46	160	24	< ADL	64
Lu	0	2	7	3	6	10	7	3	4	7	47	35	59	23	6	11	6	9	4	1	3	7	28	5	20	12
Ge[a]	0.09	0.13	3.74	3.65	3.12	2.75	3.24	5.41	4.24	3.68	6.80	5.42	5.27	4.81	3.21	4.86	3.48	4.75	4.95	5.41	4.96	3.53	6.08	4.25	12.31	6.71
Ge/Si µmol/mol			3.81	3.53	3.20	2.98	3.21	5.06	4.07	3.49	20.27	13.37	11.77	8.03	3.00	13.71	3.30	12.06	4.18	4.59	4.87	3.46	10.38	3.86	52.23	7.56
Y/Ho wt			49.0	53.9	51.4	48.3	47.6	50.6	44.3	38.7	29.0	29.4	27.2	28.7	31.7	26.3	31.3	30.2	37.9	39.6	39.8	38.4	33.6	36.2	33.9	40.6
La/La^*_{PAAS}			1.40	2.09	1.85	2.01	1.59	1.59	1.44	1.59	1.30	1.51	1.64	1.44	1.33	1.47	1.42	1.45	1.12	1.21	1.49	1.38	1.43	1.59	1.50	1.38
Ce/Ce^*_{PAAS}			0.98	1.13	1.10	1.11	1.00	0.96	0.71	1.01	1.04	1.07	1.13	1.03	1.01	1.04	1.02	0.99	0.95	0.98	1.08	1.02	1.05	1.00	1.04	0.66
Eu/Eu^*_{PAAS}			2.17	2.43	2.22	2.59	2.23	2.08	2.20	2.40	1.82	2.26	2.30	2.59	2.40	2.59	2.51	2.53	2.13	2.23	2.11	2.12	2.50	2.25	2.04	2.36
Gd/Gd^*_{PAAS}			0.94	1.35	1.17	1.41	0.94	0.89	0.97	0.92	1.16	1.28	1.21	0.91	0.88	1.14	0.85	0.89	0.76	0.76	0.84	0.91	0.92	0.83	1.17	0.92
∑REE[a]			1.69	0.61	1.16	2.89	1.49	0.62	1.03	1.10	25.80	12.70	15.48	7.33	3.95	9.00	1.90	8.15	10.17	2.18	1.53	3.31	8.21	4.13	8.58	3.41
n			3	2	3	2	4	n.a.	2	n.a.	2	n.a.	2	3	2	n.a.	3	2	3	2	n.a.	n.a.	n.a.	3	2	2
$\delta^{29}Si_{mean}$			−0.91	−0.97	−0.29	−0.38	−0.62		−0.43		−0.61		−0.63	−0.76	−1.08		−0.89	−0.77	−0.95	−0.95				−0.86	−0.75	−1.24
1 sd			0.03	0.03	0.11	0.04	0.04		0.06		0.07		0.03	0.06	0.00		0.07	0.03	0.05	0.03				0.04	0.01	0.04
$\delta^{30}Si_{mean}$			−1.75	−1.88	−0.53	−0.85	−1.30		−0.81		−1.19		−1.22	−1.39	−1.95		−1.72	−1.50	−1.76	−1.85				−1.76	−1.52	−2.27
1 sd			0.02	0.02	0.12	0.12	0.11		0.07		0.04		0.02	0.12	0.01		0.12	0.05	0.10	0.10				0.05	0.03	0.03

n.a.—not analysed.
< ADL—below analytical detection limit.
n—number of procedural replicates for isotopic analysis.
[a] Expressed in ppm.

(20 ppm) was added in both samples and standards to avoid such offsets (Hughes et al., 2011). Silicon isotope data are reported relative to the international quartz reference material NBS-28 in the delta notation as δ^{30}Si and δ^{29}Si:

$$\delta^{30,29}\mathrm{Si}(‰) = \left[\left(R_{\mathrm{sample}}/R_{\mathrm{NBS-28}}\right)-1\right] \times 1000 \quad (1)$$

where R is the ratio ^{30}Si/^{28}Si or ^{29}Si/^{28}Si in a sample and the reference material NBS-28.

The Diatomite secondary reference material was included in every sequence to check for accuracy and precision, and yielded a δ^{30}Si of $+1.26 \pm 0.07$ (1SD, $n=11$) well in agreement with the recommended value ($+1.25 \pm 0.13$; Reynolds et al., 2007).

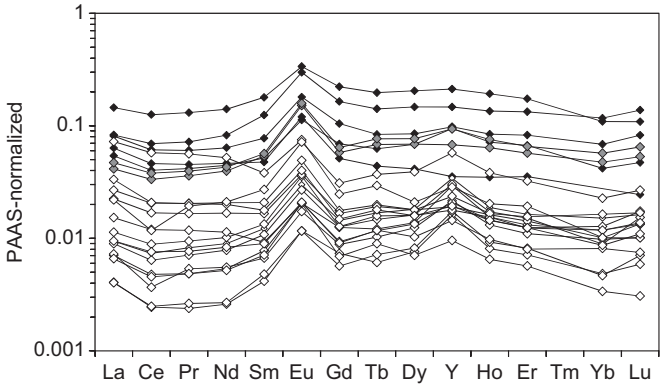

Fig. 1. PAAS-normalized REE+Y diagram comparing Si-rich mesobands (white symbols), Fe-rich mesobands (black symbols) and Si–Fe-rich mesobands (grey symbols).

4. Results

Major element concentrations are typical for Archaean BIFs, with SiO_2 and $Fe_2O_{3\ TOT}$ combined representing 84–100% (wt) of the samples, with $Fe_2O_{3\ TOT}$ ranging from 2.4 to 73% (Table 1). Based on their Si or Fe contents, mesobands will be defined as Si-rich mesobands ($>60\%$ SiO_2), Fe-rich mesobands ($>60\%$ $Fe_2O_{3\ TOT}$) or as Si–Fe-rich mesobands (subequal contents of SiO_2 and $Fe_2O_{3\ TOT}$). Al_2O_3 and MnO are present as minor elements with contents from 0 to 1.24% and 0.04 to 2.33%, respectively. Mg, Ca, Na, Ti and P are trace elements, whereas K_2O was not measurable (Table 1).

Rare earth element and Y (REE+Y) patterns of individual mesobands were normalized against Post-Archaean Australian Average Shale (PAAS; Table 1, Fig. 1). Normalized La, Ce and Eu anomalies were calculated following the methods of Bau and Dulski (1996) and Bolhar et al. (2004):

$$\mathrm{La/La^*} = \mathrm{La}/(3\mathrm{Pr}-2\mathrm{Nd}) \quad (2)$$

$$\mathrm{Ce/Ce^*} = \mathrm{Ce}/(2\mathrm{Pr}-\mathrm{Nd}) \quad (3)$$

$$\mathrm{Eu/Eu^*} = \mathrm{Eu}/(0.67\mathrm{Sm}+0.33\mathrm{Tb}) \quad (4)$$

All mesobands are characterised by positive La and Eu anomalies (1.12–2.09 and 1.82–2.59, respectively; Table 1). Y is significantly enriched in most mesobands relative to Ho (Table 1). Fe-rich and Si-Fe-rich mesobands show a very slight Y/Ho decrease upwards in the stratigraphic position (Fig. 2A), from 34.0 to 29.0. In contrast, Si-rich mesobands exhibit more variable Y/Ho (Fig. 2A), from superchondritic values (40.6; PG-9) to values close to those of shale (31.3 and 31.7 in PG-6B and 5B, respectively) in the middle of the sequence (Fig. 2A). At the top of the

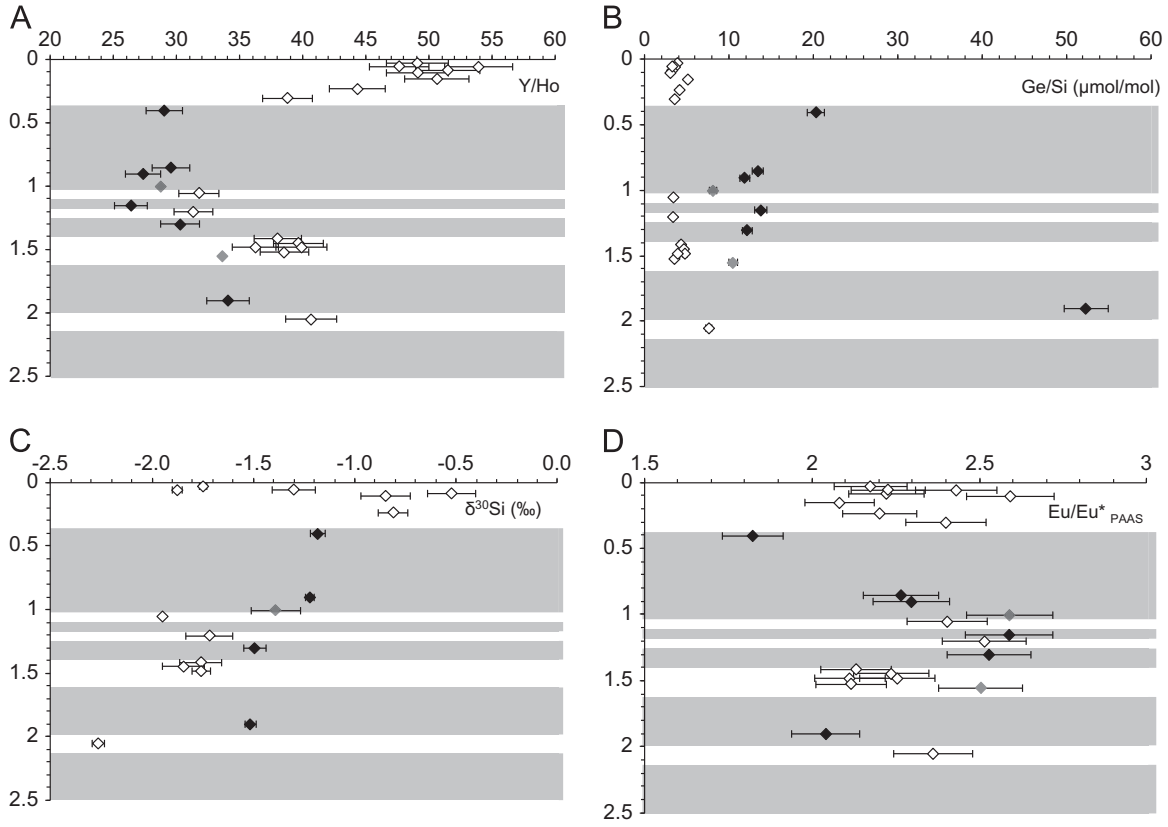

Fig. 2. Stratigraphic trends of Si-rich samples (white symbols), Fe-rich samples (black symbols) and Si–Fe-rich samples (grey symbols). (A) Y/Ho anomalies, (B) Ge/Si ratios, (C) δ^{30}Si values, (D) Eu/Eu^*_{PAAS}. Error bars represent the reproducibility ($\sim$5%). For several samples, the error bar is included within the symbol size. In case of δ^{30}Si values, symbols represent an average value and error bars are 1 sd. Grey and white areas represent Fe-rich and Si-rich layers respectively.

sequence (uppermost 0.15 m), the Y/Ho quickly reverts to higher values (47.6–53.9) close to the range of seawater (51–58; Taylor and McLennan, 1985; Alibo and Nozaki, 1999; Johannesson et al., 2006). All but two samples (PG-2C and PG-9) have no significant Ce anomalies (Table 1). Positive correlations between $\sum$REE and $Fe_2O_{3\ TOT}$ and P_2O_5 contents ($r^2=0.34$ and 0.58, respectively, with p-values <0.001; not shown) suggest that REE are hosted by Fe-oxides and phosphates minerals, likely apatite, monazite and xenotime in the order of decreasing abundances (Smith, 2007). Si-rich and Fe-rich mesobands can be distinguished on the basis of ΣREE content, as ΣREE of Fe-rich mesobands (13.29 ± 6.76 ppm) is generally higher than for Si-rich mesobands (2.57 ± 2.33 ppm) (Table 1). Lower REE contents of Si-rich mesobands relative to Fe-rich mesobands reflect the dilution of REE-bearing Fe-oxides by quartz. Moreover, Y anomalies are less positive in Fe-rich mesobands.

Ge/Si ratios in Si-rich mesobands average 4.03 ± 1.12 μmol/mol and vary from 2.98 to 7.56 μmol/mol with the purest cherts (PG-7A and PG-7B; 98% SiO_2) showing Ge/Si ratios of 4.25 and 4.59 μmol/mol, respectively (Table 1; Fig. 2B). Excluding two outliers (PG-8 and 9) there is no significant linear relation observed between Fe and Ge contents (Fig. 3). Fe-rich mesobands display higher and more variable Ge/Si ratios (11.77–52.23 μmol/mol). Typically, an increase in Ge/Si ratios is observed as the silica content decreases in favour of iron.

The Si isotope data are presented in Table 1 and Fig. 2C. δ^{30}Si values are negative and within the range previously reported for BIFs and cherts (Ding et al., 1996; André et al., 2006; Van den Boorn et al., 2007; Steinhoefel et al., 2009, 2010; Heck et al., 2011). The values exhibit regular variations relative to their position in the stratigraphic sequence (Fig. 2C), starting with pronounced negative δ^{30}Si composition at the base (PG-9, −2.27‰) followed by a continuous shift to less negative values up to −0.53‰ (PG-1C). With the exception of PG-8 (−1.52‰), δ^{30}Si values of Fe-rich mesobands follow this trend. In the uppermost 0.08 m just below the contact with overlying shale, the Si isotopic composition abruptly reverts to much more negative values (PG-1A, $\delta^{30}Si = -1.75$‰).

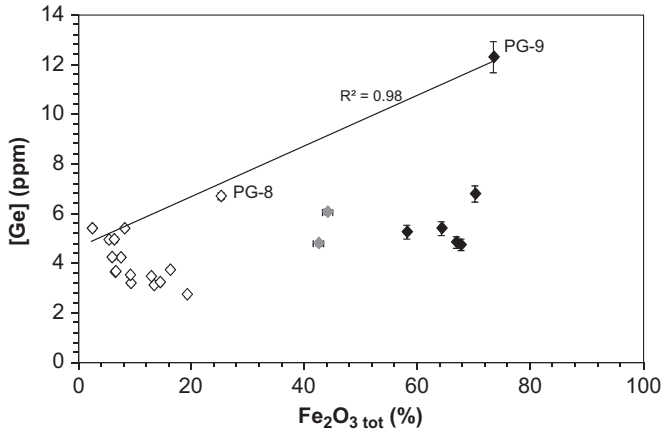

Fig. 3. Relationship between $Fe_2O_{3\ TOT}$ content (wt%) and Ge contents (ppm) of Si-rich (white symbols), Fe-rich (black symbols) and Si–Fe-rich (grey symbols) mesobands of Mozaan BIF. Black line represents the relation between Fe_2O_3 and Ge contents using data from samples PG-8 and 9 and the purest SiO_2 layers (PG-7A and 7B; 98% SiO_2) ($r^2=0.98$ with p-value$=0.007$). This relation provides evidence for adsorption processes in samples PG-8 and 9 and its absence in other samples. Adsorption processes in PG-8 can explain the higher δ^{30}Si value of this sample as adsorption of Si onto Fe-oxides is potentially accompanied by lower fractionation factors than precipitation ($^{30}\Delta_{adsorption}$ down to −1.1‰, Delstanche et al., 2009 instead of $^{30}\Delta_{solid-fluid}$ about −1.8‰, Basile-Doelsch et al., 2005; Van den Boorn et al., 2010).

5. Discussion

5.1. Clastic contamination

Before interpreting the geochemical tracers in term of depositional processes, the potential impact of a clastic contamination requires evaluation, because some samples contain Al_2O_3 contents exceeding 0.5% probably due to a clastic component. Because soil-forming processes produce clays having light silicon isotopic signatures (e.g., Ziegler et al., 2005; Opfergelt et al., 2010), a detrital contribution of weathered material may be a potential controlling factor that could account for the observed negative δ^{30}Si values. However, the absence of covariation between the isotopic signatures and the level of detrital contribution (e.g., Al_2O_3 or TiO_2 contents) in any of the examined Fe-rich or Si-rich layers demonstrates that clastic contamination did not have a significant effect on silicon isotope composition (Fig. 4A). Likewise, there is no observed correlation between Eu/Eu^* or Ge/Si and Al_2O_3 contents, suggesting a negligible effect of clastic contamination on the size of Eu anomalies (Fig. 4B) and Ge/Si (Fig. 4C).

In contrast a seawater precipitate having a superchondritic Y/Ho ratio (>50) would be very sensitive to a contamination by terrigeneous material with a low Y/Ho ratio (~26). From the negative correlation between Al_2O_3 content and Y/Ho ratios illustrated in Fig. 4D, we assume that Y/Ho ratios below 40 are controlled by clastic contamination. Considering that Al_2O_3 content is exclusively related to clastic contamination, a clastic contribution of up to ~2 wt% for Si-rich mesobands (highest Al_2O_3 content of 0.42% in PG-5B) and 6 wt% for Fe-rich mesobands (highest Al_2O_3 content of 1.24% in PG-4B) is estimated using a mass balance calculation:

$$[X]_{total} = [X]_1 \times f_1 + [X]_2 \times f_2 \quad (5)$$

with $f_1+f_2=1$,where $[X]$ is the concentration of the element X.

Using 2.95 Ga Mozaan Group shales as representative of terrigeneous material (Al_2O_3 content of ~23%; Delvigne 2012) (Fig. 4D) and postulating precipitates free of alumina. A clastic contribution limits the use of Y/Ho ratio as a tracer to qualitative interpretation. Interestingly, samples suspected to be contaminated (Al_2O_3 content above 0.1%) fall on calculated contamination trends between detritus-free samples with Y/Ho ratios about 40 and 45 (PG-9 and PG-2C, respectively) and terrigeneous material (2.95 Ga Mozaan Group shale; Delvigne 2012) (Fig. 4D). From this, we suppose that uncontaminated Y/Ho ratios of those samples are ~40 or 45 which are similar to Y/Ho ratios in surrounding detritus-free Si-rich samples (PG-2C, 2D, 7B, 7C and 9).

5.2. A common parental fluid for Fe- and Si-rich layers

Before differentiating between the processes that may have been responsible for the changes in composition in the BIF, it is important to assess whether or not Si- and Fe-rich layers could have been derived from a common parental fluid. The coevolution of δ^{30}Si signatures of both types of layers along the stratigraphy (except PG-8) strongly suggests a common parental fluid source for both types of bands. This is strengthened by similar Eu anomalies, indicating that all mesobands contain a similar proportion of high-T hydrothermal fluid in their parental fluid. Similarly, Y anomalies do not differ significantly between both types of layers taking into account uncertainties related to clastic contamination (Fig. 4D). As a result, these three tracers point to a common source for both mesobands.

However, contrasting Ge/Si ratios between Fe-rich and Si-rich layers are commonly regarded to indicate that silica and iron sources of BIF were decoupled (Hamade et al., 2003; Frei and Polat, 2007). According to these authors, high Ge/Si ratios of

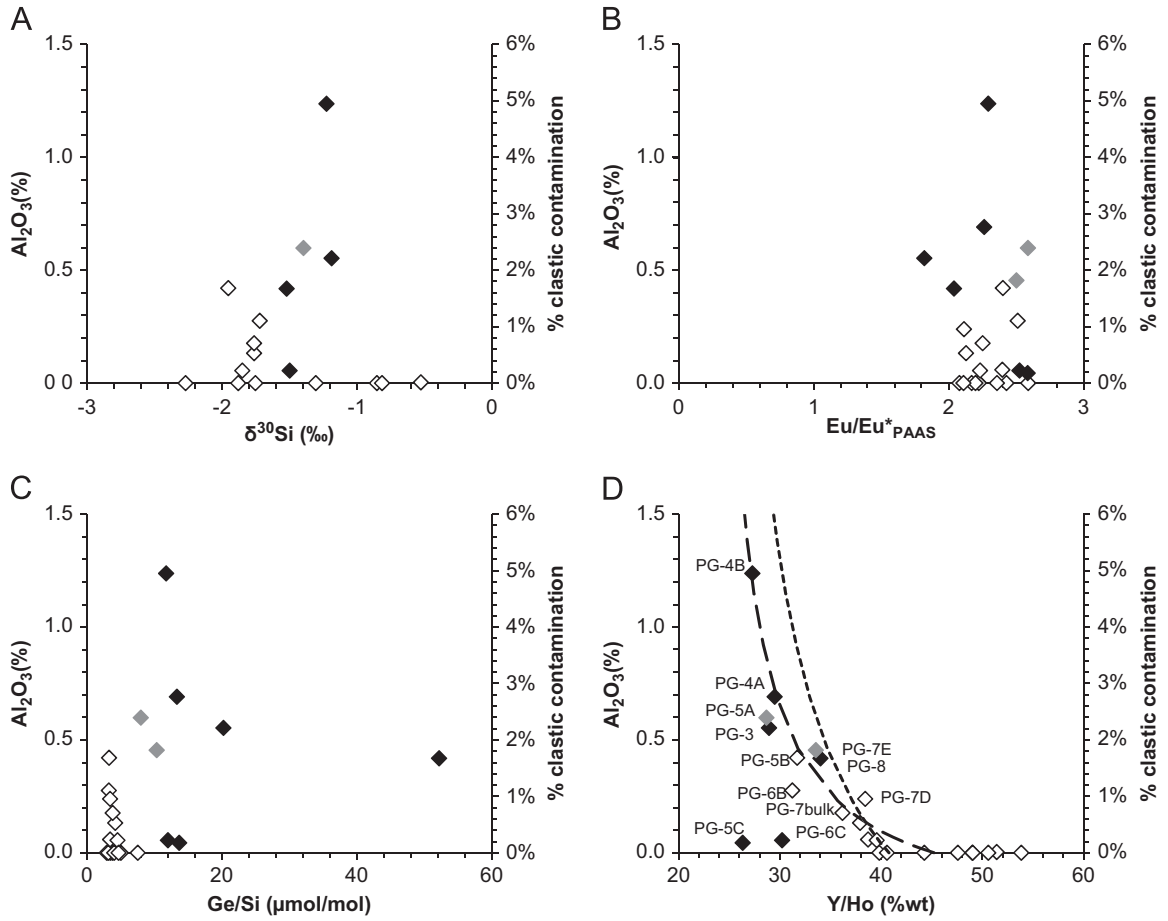

Fig. 4. Relation between Al_2O_3 (%) and percentage of clastic contamination (*y*-axes on right and left side of each diagram) and (A) $\delta^{30}Si$ values (‰), (B) Ge/Si ratios (µmol/mol), (C) Y/Ho ratios, (D) Eu/Eu^*_{PAAS} in Si-rich mesobands (white symbols), Fe-rich mesobands (black symbols) and Si–Fe-rich mesobands (grey symbols) in comparison with calculated contamination trends of detritus-free samples (Al_2O_3 content at 0%) with Y/Ho ratios about 40 (PG-9, dotted line) and 45 (PG-2C, dashed line) by terrigeneous material (2.95 Ga Mozaan shale; Delvigne 2012).

Fe-rich mesobands would be inherited from hydrothermal fluids, whereas low ratios of Si-rich mesobands would be indicative of continental inputs. To conciliate Ge/Si ratios with other tracers in favour of a common source, we propose that contrasted Ge/Si ratios between layers may result from either a preferential affinity of Ge for Fe-oxyhydroxydes relative to silicon (Pokrovsky et al., 2006) or large changes in Si contents. Ge contents are slighty higher in Fe-rich layers than in Si-rich layers (5.42 ± 0.82 versus 3.97 ± 0.85 ppm, excluding PG-8 and 9), but no positive correlation exists between Ge and Fe contents for most but two samples (PG-8 and 9; see Fig. 3 for details). Therefore, we found no evidence that the Ge sequestration by Fe-oxyhydroxides might be the major factor that controls the difference in Ge/Si between the Si and Fe-rich layers. SiO_2 concentrations are more variable (from 19.5% to 98.1%) than Ge concentrations (from 2.75 to 6.08 ppm excluding PG-8 and 9). Therefore, we infer that the changes in Ge/Si ratios between layers reflect their variable quartz proportions and are not indicative of different fluid sources.

5.3. Constraints on the common parental fluid

From the remarkable coherence of REE+Y patterns of Archaean BIFs and marine carbonates, Bolhar et al. (2005) suggested that BIFs are a faithful record of the REE+Y pattern of seawater. Impact of post-depositional processes, such as diagenesis, metamorphism and surface weathering, on the primary composition were found negligible in most cases (Bau, 1993; Bau and Dulski, 1996; Bolhar et al., 2004). With Mozaan Group BIFs, REE+Y are likely hosted by Fe-oxides and phosphates minerals. While phosphate minerals formed diagenetically, REE+Y, Fe and P were introduced syngenetically during BIF precipitation. The homogenous P_2O_5 contents indicate no large-scale reorganization of REE+Y concentrations during diagenesis (Table 1), suggesting that bulk rock REE+Y contents likely reflect the REE+Y pattern of the water mass from which the BIFs precipitated. REE+Y patterns of Mozaan BIFs display features consistent with seawater precipitates, namely positive La and Y anomalies (Table 1; Fig. 1) (e.g., Bolhar et al., 2004, 2005). The lack of a significant negative Ce anomaly (except PG-2C and PG-9) testifies that seawater was reduced even in shallow-water environments. This is in accordance with the absence of significant ocean redox stratification prior to 2.3 Ga (Planavsky et al., 2010). The samples also display pronounced positive Eu anomalies, indicating a contribution from high-T hydrothermal fluids. The magnitude of this anomaly is within the range of other Archaean BIFs (Alexander et al., 2008; Planavsky et al., 2010). In particular, our REE+Y data compare well with Mozaan BIFs investigated by Alexander et al. (2008). Although within the same range of values, we report slightly higher Eu anomalies (2.29 ± 0.19 versus 1.78 ± 0.14) and lower Y/Ho ratios (27.3–53.9 versus 31.4–65.4) compared to Alexander et al. (2008). This records slighly higher hydrothermal contributions and/or clastic contributions in our samples.

To assess the relative proportion of seawater, continental runoff and hydrothermal fluids present in the parental water reservoir from which the BIF precipitated, we compare the BIFs Eu and Y anomalies with those preserved in Archaean microbialites (Van Kranendonk et al., 2003; Kamber et al., 2004; Bolhar and Van Kranendonk, 2007). Using the uniform partition coefficients of REE+Y between microbialites and seawater determined by Webb and Kamber (2000), we compute the REE+Y contents of the Archaean open seawater from those microbialites. From a conservative mixture (Eq. (5)) between this reconstructed Archaean seawater and modern high-T hydrothermal fluids (Klinkhammer et al., 1994; Bau and Dulski, 1999; Douville et al., 1999), we argue that a contribution of less than 0.1% of high-T hydrothermal fluids is sufficient to account for the observed Eu anomalies (dashed area; Fig. 5). This is in good agreement with 1000:1 mixing ratios proposed by Klein and Beukes (1989) and Khan et al. (1996) to explain REE+Y patterns of other Precambrian BIFs. However, binary mixing of seawater and hydrothermal fluid is inconsistent with Y/Ho values (Fig. 5). This points to the existence of an additional REE+Y source. A control of Y/Ho ratios by clastic contamination can be excluded for all samples with very low Al_2O_3 and Y/Ho ratios, such as the lowermost Si-rich mesoband (PG-9, Fig. 5). This sample likely records the parental water composition at the beginning of the BIF precipitation process. This will be referred to as the initial parental water in the following discussion. Its Y/Ho ratio lower than expected from a mixture of open ocean and hydrothermal fluids strongly suggests a contribution of continent-derived freshwaters, because Archaean freshwater must have had a Y/Ho ratio as low as their modern counterparts (Y/Ho ~30, Hagedorn et al., 2011). Indeed, 2.8–2.6 Ga Fortescue stromatolites deposited in a setting with a dominant riverine input are characterised by low Y/Ho (Y/Ho ~30; Bolhar and Van Kranendonk, 2007). A rough estimate of the freshwater component can be obtained using a mass balance calculation (Eq. (5)). A significant contribution (about 10%) of freshwater to the Archaean open seawater with a contribution of 0.035% of hydrothermal fluid (dashed area; Fig. 5) is required to account for the Y/Ho ratio observed in the lowermost Si-rich mesoband (PG-9) (Fig. 5). Such contribution is very well in agreement with the significant continent-derived solute fluxes deduced from the Sm-Nd isotope systematics of the Mozaan BIF (Alexander et al., 2008). These authors evaluated that about 70% of the Nd in Mozaan BIF was derived from continental sources. As Nd contents of water dominated by riverine input are about 15 times more concentrated than open ocean (Van Kranendonk et al., 2003; Kamber et al., 2004; Bolhar and Van Kranendonk, 2007), a contribution of freshwater of about 14% is required to account for this 70% of continent-sourced Nd, which is very close to our estimate of 10%.

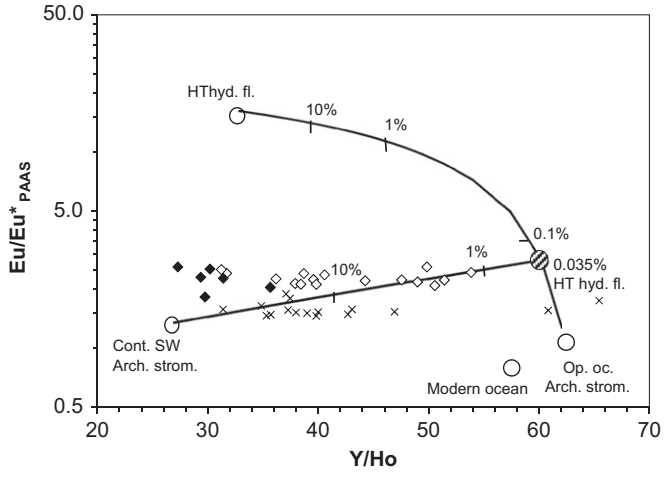

Fig. 5. Relation between Y/Ho ratios and Eu anomaly for Si-rich mesobands (white symbols) and Fe-rich mesobands (black symbols). For comparison, ~2.95 Ga Mozaan BIFs (diagonal cross; Alexander et al., 2008) are reported. Various reservoirs include modern high-temperature hydrothermal fluids (HT hyd. fl.; Klinkhammer et al., 1994; Bau and Dulski, 1999; Douville et al., 1999), modern ocean (Taylor and McLennan, 1985; Alibo and Nozaki, 1999), Archaean stromatolites precipitated in open ocean (Op. oc. Arch. Strom.; Van Kranendonk et al., 2003; Kamber et al., 2004) and Archaean stromatolites precipitated in setting with a dominant freshwater input (Cont. SW Arch. Strom.; Bolhar and Van Kranendonk, 2007). Two-component mixing lines between hydrothermal fluids and reconstructed Archaean open ocean (thin black line) and between this Archaean open ocean with a 0.035% hydrothermal contribution (dashed area) and reconstructed Archaean freshwater inputs (bold black lines) are represented. See text for details.

5.4. A common siliceous ferric oxyhydroxide precursor

Si-rich mesobands are principally made of microquartz, which is generally considered to have formed by recrystallisation of amorphous silica during diagenesis through dissolution-precipitation processes (Knauth, 1994; Marin et al., 2010). In the case of BIF, such amorphous silica precipitation might have occurred directly from seawater or through Si adsorption onto Fe-oxyhydroxides forming a siliceous ferric oxyhydroxide precursor (Maliva et al., 2005; Fischer and Knoll, 2009). A necessary condition for amorphous silica precipitation is silica oversaturation of the parental fluid that should be maintained during BIF precipitation. Although Si fluxes issued from continent-derived freshwater may have been important (Delvigne 2012), such runoff was unlikely silica-saturated because it was fed by soil-solutions in equilibrium with neoformed silicates, such as smectites and kaolinites (Delvigne 2012). Then, the freshwater contribution must have lowered the Si concentration of the seawater. Besides, the BIF precipitation itself must have depleted the Si contents of the water reservoir (the Si depletion induced by BIF precipitation is estimated about 40%, see Section 5.5 for details). Therefore, we consider a direct amorphous silica precipitation unlikely. In contrast, as envisioned by Fischer and Knoll (2009), silica could have been extensively extracted from water by a Si adsorption onto Fe-oxyhydroxides since Fein et al. (2002) have shown that a high proportion of silica (above equimolar Si/Fe ratio; Davis et al., 2001) can be bound onto Fe-oxyhydroxides even in solutions undersaturated with respect to silica. During early diagenesis, the desorbed Si must have been concentrated in the pore fluids, expelled at the water–sediment interface where a fraction of the dissolved silica may be released back into the ocean, while another would precipitate as new Si-rich layer through a local oversaturation and ultimately transform into early diagenetic chert. Although $^{30}\varepsilon_{solid-fluid}$ is not yet experimentally constrained, light isotopes will concentrate in the precipitate. Therefore, the Si released back to ocean would be ^{30}Si-enriched, potentially increasing the δ^{30}Si signature of the parental water at the water–sediment interface. Therefore, this early diagenesis might be one of the causes of the stratigraphic change in δ^{30}Si (see Section 5.5).

5.5. Sedimentary-diagenetic controls of the temporal δ^{30}Si trend

The compositional evolution of the Si-rich mesobands can be described in two stages. During the first stage (from bottom up to 0.08 m), which is recorded in the lower to middle part of the studied section, silicon isotopic signatures become heavier with no systematic changes in values of the Eu anomaly (Fig. 2). The temporal evolution of Y/Ho ratios is more uncertain as Y/Ho ratios below 40 are probably controlled by clastic contamination. However, as discussed earlier, Y/Ho ratios of the parental seawater

probably varied between 40 and 45 without changing through time. The second stage is restricted to the very top of the sequence (above 0.08 m), just before the onset of detrital sedimentation. This phase is characterised by a sharp return to negative δ^{30}Si signatures and higher Y/Ho ratios, but unchanged Eu anomalies (Fig. 2).

There are two potential explanations for increasing δ^{30}Si stratigraphically upward: (1) gradual mixing with a fluid with heavier δ^{30}Si signature; (2) a progressive ^{28}Si depletion and/or ^{30}Si enrichment through successive sedimentary and diagenetic isotopic fractionation processes.

The persistency of very similar Eu anomalies throughout the sequence (Fig. 2D) indicates that the contribution of hydrothermal fluid to parental fluid did not change significantly during the process of BIF precipitation, a feature that has also been observed for BIF from Isua (André et al., 2006). Moreover, light δ^{30}Si signatures of hydrothermal fluids (about -0.3‰; De La Rocha et al., 2000) would not account for increasing δ^{30}Si signatures of the parental water reservoir. In contrast, Archaean seawater and continent-derived freshwaters are generally thought to have had heavy δ^{30}Si signatures (between $+0.5$ and $+2$‰ and $+0.27$ and ± 0.35‰, respectively; Robert and Chaussidon, 2006; Steinhoefel et al., 2010; Van den Boorn et al., 2010; Abraham et al., 2011; Delvigne 2012). Therefore, gradual mixing between seawater with a significant freshwater contribution and open-ocean may be the mechanism responsible for increasing δ^{30}Si values upward in the sequence. Although the relative contributions of both fluids cannot accurately be assessed from Y/Ho ratios, this tracer does not support such a hypothesis. Indeed, detritus-free samples with contrasted δ^{30}Si values (e.g., PG-1B and 1C with δ^{30}Si values at -0.53‰ and -1.88‰, respectively) do not show significant changes in their Y/Ho ratios (51.4 and 53.9, respectively). In contrast, isotope fractionation processes appear as the most likely operating mechanisms and may have occurred during the following four successive steps: (1) the adsorption of Si onto Fe-oxyhydroxides generating siliceous ferric oxyhydroxides particles; (2) the desorption of Si during early diagenesis; (3) the silica precipitation as diagenetic mineral phases from the expelled pore fluid at the sediment–water interface; (4) the diagenetic silica conversion into microquartz. A fractionation of about -1.4 ± 0.3‰ has been reported for Si adsorption onto Fe-oxyhydroxides (Delstanche et al., 2009). During early diagenesis no isotopic fractionation is expected as the Si desorption is thought to fully release all fixed Si (Fischer and Knoll, 2009). The expelled Si silica would become concentrated in the pore fluid and ultimately precipitate with a $^{30}\Delta_{\text{solid–fluid}}$ between -1.5 and -2.2‰ (Basile-Doelsch et al., 2005; Van den Boorn et al., 2010) at the sediment–water interface. Upon burial diagenesis, silica conversion of amorphous silica into microquartz through dissolution–recrystallisation processes may have induced microscale δ^{30}Si variations following processes similar to the one proposed by Marin et al. (2010) and Marin-Carbonne et al. (2011). This raises the question whether or not such processes could have produces the observed stratigraphic changes in the δ^{30}Si at the outcrop scale. Two observations are at variance with such a hypothesis, the sharp return to very negative signatures at the top of the BIF sequence on the one hand and the lack of cm-scale δ^{30}Si variations within the tiny sub-sampling of the PG-7 layer (Table 1) on the other hand. Then, dissolution–recrystallisation processes may have induced microscale δ^{30}Si variations but without cm-scale reorganization. Therefore, of these four steps, two likely involve Si isotope fractionation and both result in an increase in the δ^{30}Si of the parental water reservoir. During Si adsorption onto Fe-oxyhydroxides, the parental fluid will be progressively ^{28}Si-depleted following a Rayleigh-like distillation process. Note that such a Rayleigh system is compatible with Si inputs from open ocean and/or continental inputs when Si exports exceed Si inputs (Fry, 2006). Indeed, a Rayleigh distillation process may develop because there is successive use of the same reservoir and repeated product formation from the dwindling reservoir pool. In the very top part of the section, the sharp decrease to very negative δ^{30}Si signatures points to a Si export/Si input ratio below 1 ending the Rayleigh system.

So far the fractionation factor associated with the equilibrium precipitation of silica from a fluid ($\varepsilon_{\text{solid–fluid}}$) has not been established experimentally. However, fractionations of about -1.5‰ and -2.2‰ have been estimated from natural occurrences (Basile-Doelsch et al., 2005; Van den Boorn et al., 2010). Then, the silicon released back to ocean is likely strongly ^{30}Si-enriched. To better apprehend the evolution of the parental water reservoir, we merge the two fractionation processes into one fractionation step with a bulk cumulative fractionation between the parental water and microquartz of about -3.2 ± 0.7‰. We then assume that the parental water reservoir evolved following a Rayleigh-like distillation process. Using this fractionation factor together with the Si isotope composition of the first precipitated Si-rich mesoband (δ^{30}Si$= -2.27$‰, Table 1) provides an estimate of the δ^{30}Si signature of the initial parental water of $+0.9 \pm 0.7$‰. Moreover, the heaviest δ^{30}Si signatures may correspond to a depletion of about 40% of the dissolved Si present in the initial parental water.

6. Conclusion

A 3 m thick horizon of BIF from the Mesoarchaean Mozaan Group displays characteristic geochemical and isotopic features of a precipitate from a seawater reservoir strongly affected by continent-derived freshwaters ($\sim$10%) mixed with open ocean and minor (<0.1%) high-T hydrothermal fluid. Silicon isotopes, Ge/Si ratio and REE+Y point to a common parental water reservoir for both Fe- and Si-rich layers and favour the hypothesis of Si precipitation promoted by Si adsorption onto Fe-oxyhydroxides (Fischer and Knoll, 2009). We propose two steps of Si isotope fractionation in the model of BIF deposition envisioned by Fischer and Knoll (2009). The first one occurs during Si adorption onto Fe-oxyhydroxide precursor with a $^{30}\varepsilon$ of -1.4 ± 0.3‰ inducing a gradual ^{28}Si-depletion in the parental water reservoir. The second one takes place during early diagenesis when a part of the desorbed silicon is released back into the ocean with a heavy δ^{30}Si signature and was precipitated as a silica-rich layer due to a local silica-oversaturation at the sediment–water interface. Then, both processes concur to increase the δ^{30}Si value of the parental water reservoir producing the observed gradual stratigraphic changes in the δ^{30}Si signatures of both Si and Fe-rich layers

Acknowledgements

We greatly thank J. Navez, L. Monin, N. Dahkani (MRAC) for laboratory assistance, and N. Mattielli and J. de Jong (ULB) for managing the MC-ICP-MS facility in ULB. The manuscript has greatly benefited from the constructive comments of T.M. Harrison, the reviews of J. Marin-Carbonne and M. Chaussidon and one anonymous referee. C.D. is supported by the "Fonds pour la formation à la Recherche dans l'Industrie et dans l'Agriculture" (FRIA) of Belgium and D.C. by the Federal Belgian Science Policy. AH acknowledges support by the National Research Foundation of South Africa. The NuPlasma facility has been acquired through funding by the Fonds National de la Recherche Scientifique (FNRS) (FRFC 2.4.512.00F). Additional funding was provided by the FNRS for running the Plasma Mass Spectrometer Facility Community (FRFC 2.4579.04).

References

Abraham, K., Opfergelt, S., Fripiat, F., Cavagna, A., de Jong, J., Foley, S., André, L., Cardinal, D., 2008. δ^{30}Si and δ^{29}Si determinations on USGS BHVO-1 and BHVO-2 reference materials with a new configuration on a Nu Plasma Multi-Collector ICP-MS. Geostand. Geoanal. Res. 32, 193–202.

Abraham, K., Hofmann, A., Foley, S.F., Cardinal, D., Harris, C., Barth, M., André, L., 2011. Coupled silicon–oxygen isotope fractionation traces Archaean silicification. Earth Planet. Sci. Lett. 301, 222–230.

Alexander, B., Bau, M., Andersson, P., Dulski, P., 2008. Continentally-derived solutes in shallow Archean seawater: rare earth element and Nd isotope evidence in iron formation from the 2.9 Ga Pongola Supergroup, South Africa. Geochim. Cosmochim. Acta 72, 378–394.

Alibo, D.S., Nozaki, Y., 1999. Rare earth elements in seawater: particle association, shale-normalization, and Ce oxidation. Geochim. Cosmochim. Acta 63, 363–372.

André, L., Cardinal, D., Alleman, L., Moorbath, S., 2006. Silicon isotopes in ~3.8 Ga West Greenland rocks as clues to the Eoarchaean supracrustal Si cycle. Earth Planet. Sci. Lett. 245, 162–173.

Aries, S., Valladon, M., Polvé, M., Dupré, B., 2000. A routine method for oxide and hydroxide interference corrections in ICP-MS chemical analysis of environmental and geological samples. Geostand. Newsl. 24, 19–31.

Basile-Doelsch, I., Meunier, J., Parron, C., 2005. Another continental pool in the terrestrial silicon cycle. Nature 433, 399–402.

Bau, M., 1993. Effects on syn- and post-depositional processes on rare-earth element distribution in Precambrian iron formations. Eur. J. Mineral. 5, 257–267.

Bau, M., Dulski, P., 1996. Distribution of yttrium and rare-earth elements in the Penge and Kuruman iron-formations, Transvaal Supergroup, South Africa. Precambrian Res. 79, 37–55.

Bau, M., Dulski, P., 1999. Comparing yttrium and rare earths in hydrothermal fluids from the Mid-Atlantic Ridge: implications for Y and REE behaviour during near-vent mixing and for the Y/Ho ratio of Proterozoic seawater. Chem. Geol. 155, 77–90.

Bau, M., Möller, P., 1993. Rare earth element systematics of the chemically precipitated component in Early Precambrian iron formations and the evolution of the terrestrial atmosphere–hydrosphere–lithosphere system. Geochim. Cosmochim. Acta 57, 2239–2249.

Bekker, A., Slack, J.F., Planavsky, N., Krapez, B., Hofmann, A., Konhauser, K.O., Rouxel, O.J., 2010. Iron formation: the sedimentary product of a complex interplay among Mantle, Tectonic, Oceanic, and Biospheric processes. Econ. Geol. 105, 467–508.

Beukes, N.J., Cairncross, B., 1991. A lithostratigraphic sedimentological reference profile for the late Archaean Mozaan Group, Pongola Sequence: application to sequence stratigraphy and correlation with the Witwatersrand Supergroup. S. Afr. J. Geol. 94, 44–69.

Bolhar, R., Kamber, B., Moorbath, S., Fedo, C., Whitehouse, M., 2004. Characterisation of early Archaean chemical sediments by trace element signatures. Earth Planet. Sci. Lett. 222, 43–60.

Bolhar, R., Van Kranendonk, M.J., Kamber, B., 2005. A trace element study of siderite-jasper banded iron formation in the 3.45 Ga Warrawoona Group, Pilbara Craton—formation from hydrothermal fluids and shallow seawater. Precambrian Res. 137, 93–114.

Bolhar, R., Van Kranendonk, M., 2007. A non-marine depositional setting for the northern Fortescue Group, Pilbara Craton, inferred from trace element geochemistry of stromatolitic carbonates. Precambrian Res. 155, 229–250.

Braterman, P.S., Cairns-Smith, A.G., Sloper, R.W., 1983. Photo-oxidation of hydrated Fe^{2+} significance for banded iron formations. Nature 303, 163–164.

Cairns-Smith, A.G., 1978. Precambrian solution photochemistry, inverse segregation, and banded iron formations. Nature 76, 807–808.

Cardinal, D., Alleman, L., de Jong, J., Ziegler, K., André, L., 2003. Isotopic composition of silicon measured by multicollector plasma source mass spectrometry in dry plasma mode. J. Anal. At. Spectrom. 18, 213–218.

Cloud, P., 1965. Significance of the Gunflint (Precambrian) microflora. Science 148, 27–35.

Cloud, P., 1973. Paleoecological significance of the banded iron formation. Econ. Geol. 68, 1135–1143.

Davis, C.C., Knocke, W.F., Edwards, M., 2001. Implications of aqueous silica sorption to iron hydroxide: mobilization of iron colloids and interference with sorption of arsenate and humic substances. Environ. Sci. Technol. 35, 3158–3162, http://dx.doi.org/10.1021/es0018421.

De La Rocha, C.L., Brzezinski, M.A., DeNiro, M.J., 2000. A first look at the distribution of the stable isotopes of silicon in natural waters. Geochim. Cosmochim. Acta 64, 2467–2477.

Delstanche, S., Opfergelt, S., Cardinal, D., Elsass, F., André, L., Delvaux, B., 2009. Silicon isotopic fractionation during adsorption of aqueous monosilicic acid onto iron oxide. Geochim. Cosmochim. Acta 73, 923–934.

Delvigne, C., 2012. The Archaean silicon cycle Insights from silicon isotopes and Ge/Si ratios in banded iron formations, palaeosols and shales. Ph.D. Thesis. Université Libre de Bruxelles. 181 pp.

Derry, L., Jacobsen, S., 1990. The chemical evolution of Precambrian seawater—evidence from REEs in banded iron formations. Geochim. Cosmochim. Acta 54, 2965–2977.

Ding, T., Jiange, S., Wan, D., Li, Y., Li, J., Song, H., Liu, Z., Yao, X., 1996. Silicon Isotope Geochemistry. Geological Publishing House, Beijing, China.

Dix, O.R., 1984. Early Proterozoic braided stream, shelf and tidal deposition in the Pongola Sequence, Zululand. Trans. Geol. Soc. S. Afr 87, 1–10.

Douville, E., Bienvenu, P., Charlou, J.-L., Donval, J.-P., Fouquet, Y., Appriou, P., Gamo, T., 1999. Yttrium and rare earth elements in fluids from various deep-sea hydrothermal systems. Geochim. Cosmochim. Acta 63, 627–643.

Evans, M.J., Derry, L.A., 2002. Quartz control of high germanium/silicon ratios in geothermal waters. Geology 30, 1019–1022.

Fein, J.B., Scott, S., Rivera, N., 2002. The effect of Fe and Si adsorption on *Bacillus subtilis* cell walls: insights into non-metabolic bacterial precipitation of silicate minerals. Chem. Geol. 182, 265–273, http://dx.doi.org/10.1016/S0009-2541(01)00294-7.

Fischer, W.W., Knoll, A.H., 2009. An iron shuttle for deepwater silica in late Archean and early Paleoproterozoic iron formation. GSA Bull. 121, 222–235.

Fitoussi, C., Bourdon, B., Kleine, T., Oberli, F., Reynolds, B.C., 2009. Si isotope systematics of meteorites and terrestrial peridotites: implications for Mg/Si fractionation in the solar nebula and for Si in the Earth's core. Earth Planet. Sci. Lett. 287, 77–85.

Frei, R., Polat, A., 2007. Source heterogeneity for the major components of similar to 3.7 Ga banded iron formations (Isua Greenstone Belt, Western Greenland): tracing the nature of interacting water masses in BIF formation. Earth Planet. Sci. Lett. 253, 266–281.

Froelich, P.N., Blanc, V., Mortlock, R.A., Chilrud, S.N., Dunstan, W., Udomkit, A., Peng, T.-H., 1992. River fluxes of dissolved silica to the ocean were higher during glacials: Ge/Si in diatoms, rivers and oceans. Paleoceanography 7, 739–767.

Fry, B., 2006. Stable Isotope Ecology. Springer, New York (pp. 308).

Garrels, R.M., 1987. A model for the deposition of the microbanded Precambrian iron formations. Am. J. Sci. 287, 81–106.

Georg, R.B., Reynolds, B.C., Frank, M., Halliday, A.N., 2006. New sample preparation techniques for the determination of Si isotopic compositions using MC-ICPMS. Chem. Geol. 235, 95–104.

Hagedorn, B., Cartwright, I., Raveggi, M., Maas, R., 2011. Rare earth element and strontium geochemistry of the Australian Victorian Alps drainage system: evaluating the dominance of carbonate vs. aluminosilicate weathering under varying runoff. Chem. Geol. 284, 105–126.

Hamade, T., Konhauser, K., Raiswell, R., Goldsmith, S., Morris, R., 2003. Using Ge/Si ratios to decouple iron and silica fluxes in Precambrian banded iron formations. Geology 31, 35–38.

Hammerbeck, E.C.I., 1977. The Usushwana Complex in the Southeastern Transvaal with Special References to its Economic Potential. Ph.D. Thesis (unpublished), Univ. Pretoria, 226pp.

Heck, P.R., Huberty, J.M., Kita, N.T., Ushikubo, T., Kozdon, R., Valley, J.W., 2011. SIMS analyses of silicon and oxygen isotope ratios for quartz from Archean and Paleoproterozoic banded iron formations. Geochim. Cosmochim. Acta 75, 5879–5891.

Hegner, E., Kröner, A., Hunt, P., 1994. A precise U–Pb zircon age for the Archaean Pongola Supergroup volcanics in Swaziland. J. Afr. Earth Sci. 18, 339–341.

Hughes, H.H., Delvigne, C., Korntheuer, M., de Jong, J., André, L., Cardinal, D., 2011. Controlling the mass bias introduced by anionic and organic matrices in silicon isotopic measurements by MC-ICP-MS. J. Anal. At. Spectrom. 26, 1892–1896.

Jacobsen, S.B., Pimentel-Klose, M.R., 1988. Nd isotopic variations in Precambrian banded iron formations. Geophys. Res. Lett. 15, 393–396.

Johannesson, K.H., Hawkins, D.L., Cortés, A., 2006. Do Archean chemical sediments record ancient seawater rare earth element patterns? Geochim. Cosmochim. Acta 70, 871–890.

Kamber, B.S., Bolhar, R., Webb, G.E., 2004. Geochemistry of late Archaean stromatolites from Zimbabwe: evidence for microbial life in restricted epicontinental seas. Precambrian Res. 132, 379–399.

Kappler, A., Pasquero, C., Konhauser, K.O., Newman, D.K., 2005. Deposition of banded iron formations by anoxygenic phototrophic Fe(II)-oxidizing bacteria. Geology 33, 865–868.

Khan, R.M.K., Das Sharma, S., Patil, D.J., Naqvi, S.M., 1996. Trace, rare-earth element, and oxygen isotopic systematics for the genesis of banded iron-formations: evidence from the Kushtagi schist belt, Archaean Dharwar Craton, India. Geochim. Cosmochim. Acta 60, 3285–3294.

Klein, C., Beukes, N.J., 1989. Geochemistry and sedimentology of a facies transition from limestone to iron-formation deposition in the early Proterozoic Transvaal Supergroup, South Africa. Econ. Geol. 84, 1733–1774.

Klinkhammer, G.P., Elderfield, H., Edmond, J.M., Mitra, A., 1994. Geochemical implications of rare earth element patterns in hydrothermal fluids from mid-ocean ridges. Geochim. Cosmochim. Acta 58, 5105–5113.

Knauth, L.P., 1994. Petrogenesis of chert Silica: physical behavior, geochemistry and materials applications. In: Heaney, P.J. (Ed.), Mineralogical Society of America, pp. 233–258.

Konhauser, K.O., Hamade, T., Raiswell, R., Morris, R.C., Ferris, F.G., Southam, G., Canfield, D.E., 2002. Could bacteria have formed the Precambrian banded iron formations? Geology 30, 1079–1082.

Lascelles, D.F., 2007. Black smokers and density currents: a uniformitarian model for the genesis of banded iron-formations. Ore Geol. Rev. 32, 381–411.

Linström, W., 1987. Die geologie van die gebeid Vryheid. Explan. Sheet 2730. Geological Survey of South Africa (48pp).

Maliva, R.G., Knoll, A.H., Simonson, B.M., 2005. Secular change in the Precambrian silica cycle: insights from chert petrology. Geol. Soc. Am. Bull. 117, 835–845, http://dx.doi.org/10.1130/B25555.1.

Marin, J., Chaussidon, M., Robert, F., 2010. Microscale oxygen isotope variations in 1.9 Ga Gunflint cherts: assessments of diagenesis effects and implications for oceanic paleotemperature reconstructions. Geochim. Cosmochim. Acta 74, 116–130.

Marin-Carbonne, J., Chaussidon, M., Boiron, M.-C., Robert, F., 2011. A combined in situ oxygen, silicon isotopic and fluid inclusion study of a chert sample from Onverwacht Group (3.35 Ga, South Africa): new constraints on fluid circulation. Chem. Geol. 286, 59–71.

Matthews, P.E., 1967. The pre-Karroo formations of the White Umfolozi inlier, northern Natal. Trans. Geol. Soc. S. Afr. 70, 39–63.

Morris, R.C., 1993. Genetic modeling for banded iron-formation of the Hamersley Group, Pilbara Craton, Western Australia. Precambrian Res. 60, 243–286.

Mortlock, R.A., Froelich, P.N., Feely, R.A., Massoth, G.J., Butterflield, D.A., Lupton, J.E., 1993. Silica and germanium in Pacific Ocean hydrothermal vents and plumes. Earth Planet. Sci. Lett. 119, 365–378.

Opfergelt, S., Cardinal, D., André, L., Delvigne, C., Bremond, L., Delvaux, B., 2010. Variations of d^{30}Si and Ge/Si with weathering and biogenic input in tropical basaltic ash soils under monoculture. Geochim. Cosmochim. Acta 74, 225–240.

Planavsky, N., Bekker, A., Rouxel, O.J., Kamber, B., Hofmann, A., Knudsen, A., Lyons, T.W., 2010. Rare earth element and yttrium compositions of Archean and Paleoproterozoic Fe formations revisited: new perspectives on the significance and mechanisms of deposition. Geochim. Cosmochim. Acta 74, 6387–6405.

Pokrovsky, O.S., Pokrovski, G.S., Schott, J., Galy, A., 2006. Experimental study of germanium adsorption on goethite and germanium coprecipitation with iron hydroxide: X-ray absorption fine structure and microscopic characterization. Geochim. Cosmochim. Acta 70, 3325–3341.

Posth, N.R., Hegler, F., Konhauser, K.O., Kappler, A., 2008. Alternating Si and Fe deposition caused by temperature fluctuations in Precambrian oceans. Nat. Geosci. 1, 703–708, http://dx.doi.org/10.1038/ngeo306.

Reimold, W.U., Meyer, F.M., Walraven, F., Matthews, P.E., 1993. Geochemistry and chronology of pre- and post-Pongola granitoids from northeastern Natal. In: Maphalala, R., Mabuza, M. (Eds.), Extended Abstracts: 16th International Colloquium on African Geology. Geol. Surv. Mines Dep., Swaziland, pp. 294–296.

Reynolds, B., Aggarwal, J., André, L., Baxter, D., Beucher, C., Brzezinski, M., Engström, E., Georg, R., Land, M., Leng, M., Opfergelt, S., Rodushkin, I., Sloane, H.J., Van den Boorn, S.H.J.M., Vroon, P.Z., Cardinal, D., 2007. An inter-laboratory comparison of Si isotope reference materials. J. Anal. At. Spectrom. 22, 561–568.

Robert, F., Chaussidon, M., 2006. A palaeotemperature curve for the Precambrian oceans based on silicon isotopes in cherts. Nature 443, 969–972, http://dx.doi.org/10.1038/nature05239.

Robinson, P., Townsend, A.T., Yu, Z., Münker, C., 1999. Determination of Scandium, Yttrium and Rare Earth elements in rocks by High Resolution Inductively Coupled Plasma-Mass Spectrometry. Geostand. Newsl. 23, 31–46.

Siever, R., 1992. The silica cycle in the Precambrian. Geochim. Cosmochim. Acta 56, 3265–3272.

Smith, A.J.B., 2007. The Paleo-Environmental Significance of the Iron-Formations and Iron-Rich Mudstones of the Mesoarchean Witwatersrand-Mozaan Basin, South Africa. MSc Thesis, University of Johannesburg, pp. 208.

Steinhoefel, G., Horn, I., von Blanckenburg, F., 2009. Micro-scale tracing of Fe and Si isotope signatures in banded iron formation using femtosecond laser ablation. Geochim. Cosmochim. Acta 73, 5343–5360.

Steinhoefel, G., von Blanckenburg, F., Horn, I., Konhauser, K.O., Beukes, N.J., Gutzmer, J., 2010. Deciphering formation processes of banded iron formations from the Transvaal and the Hamersley successions by combined Si and Fe isotope analysis using UV femtosecond laser ablation. Geochim. Cosmochim. Acta 74, 2677–2696.

Tankard, A.J., Jackson, M.P.A., Eriksson, K.A., Hobday, D.K., Hunter, D.R., Minter, W.E.L., 1982. Crustal Evolution of Southern Africa. Springer Verlag, New York.

Taylor, S.R., McLennan, S.M., 1985. The Continental Crust: Its Composition and Evolution. Blackwell Scientific, Oxford.

Van den Boorn, S., van Bergen, M., Nijman, W., Vroon, P., 2007. Dual role of seawater and hydrothermal fluids in Early Archean chert formation: evidence from silicon isotopes. Geology 35, 939–942.

Van den Boorn, S., Vroon, P.Z., van Bergen, M., 2009. Sulphur-induced offsets in MC-ICP-MS silicon-isotopes measurements. J. Anal. At. Spectrom. 24, 1111–1114.

Van den Boorn, S., van Bergen, M., Vroon, P., de Vries, S., Nijman, W., 2010. Silicon isotope and trace element constraints on the origin of ~3.5 Ga cherts: implications for early archaean marine environments. Geochim. Cosmochim. Acta 74, 1077–1103.

Van Kranendonk, M.J., Webb, G.E., Kamber, B.S., 2003. Geological and trace element evidence for a marine sedimentary environment of deposition and biogenicity of 3.45 Ga stromatolitic carbonates in the Pilbara craton, and support for a reducing Archaean ocean. Geobiology 1, 91–108.

von Brunn, V., Mason, T.R., 1977. Siliciclastic-carbonate tidal deposits from the 3000 M.Y. Pongola Supergroup, South Africa. Sediment. Geol. 18, 245–255.

Wang, Y., Xu, H., Merino, E., Konishi, H., 2009. Generation of banded iron formations by internal dynamics and leaching of oceanic crust. Nat. Geosci. 2, 781–784.

Webb, G.E., Kamber, B.S., 2000. Rare earth elements in Holocene reefal microbialites: a new shallow seawater proxy. Geochim. Cosmochim. Acta 64, 1557–1565.

Ziegler, K., Chadwick, O., Brzezinski, M., Kelly, E., 2005. Natural variations of δ^{30}Si ratios during progressive basalt weathering, Hawaiian Islands. Geochim. Cosmochim. Acta 69, 4597–4610.